nature geoscience

Article

https://doi.org/10.1038/s41561-023-01175-6

Direct observation of Earth's spectral long-wave feedback parameter

Received: 19 May 2022

Accepted: 25 March 2023

Published online: 20 April 2023

Check for updates

Florian E. Roemer[1,2] ✉, Stefan A. Buehler[1], Manfred Brath[1], Lukas Kluft[3] & Viju O. John[4]

The spectral long-wave feedback parameter represents how Earth's outgoing long-wave radiation adjusts to temperature changes and directly impacts Earth's climate sensitivity. Most research so far has focused on the spectral integral of the feedback parameter. Spectrally resolving the feedback parameter permits inferring information about the vertical distribution of long-wave feedbacks, thus gaining a better understanding of the underlying processes. However, investigations of the spectral long-wave feedback parameter have so far been limited mostly to model studies. Here we show that it is possible to directly observe the global mean all-sky spectral long-wave feedback parameter using satellite observations of seasonal and interannual variability. We find that spectral bands subject to strong water-vapour absorption exhibit a substantial stabilizing net feedback. We demonstrate that part of this stabilizing feedback is caused by the change of relative humidity with warming, the radiative fingerprints of which can be directly observed. Therefore, our findings emphasize the importance of better understanding processes affecting the present distribution and future trends in relative humidity. This observational constraint on the spectral long-wave feedback parameter can be used to evaluate the representation of long-wave feedbacks in global climate models and to better constrain Earth's climate sensitivity.

The long-wave feedback parameter λ indicates how Earth's outgoing long-wave radiation $\mathcal{L}$ responds to changes in near-surface air temperature T_s and thus directly affects Earth's climate sensitivity. Despite extensive research on λ throughout the past decades, the bulk of that research has focused on its spectrally integrated value[1–4]. However, radiative feedbacks—and thus λ—fundamentally possess a spectral dimension. Therefore, we use satellite observations to directly infer Earth's spectral long-wave feedback parameter

$$\lambda_\nu = -\frac{\mathrm{d}\mathcal{L}_\nu}{\mathrm{d}T_s} \quad (1)$$

where $\mathcal{L}_\nu$ is the spectral outgoing long-wave radiation. In this framework, stabilizing feedbacks are negative and amplifying feedbacks are positive.

Spectrally resolving λ_ν offers clear advantages compared with considering only the spectrally integrated λ. First, the absorption of long-wave radiation by different atmospheric species strongly varies with wavenumber ν, making it possible to directly attribute changes in $\mathcal{L}_\nu$ to the responsible absorbing species. Second, the spectrally varying absorption strength also causes strong variations in the emission level, the vertical layer $\mathcal{L}_\nu$ is most sensitive to. This makes it possible to infer information about the vertical distribution of long-wave feedbacks. By considering only the integrated λ, this information can be lost due to cancelling effects in different spectral bands[5–8].

The use of spectrally resolved satellite observations to study λ_ν was already suggested by Madden and Ramanathan[9]. However, the lack of hyperspectral satellite instruments with a sufficiently long time series

[1]Center for Earth System Research and Sustainability (CEN), Meteorological Institute, Universität Hamburg, Hamburg, Germany. [2]International Max Planck Research School on Earth System Modelling (IMPRS-ESM), Hamburg, Germany. [3]Max Planck Institute for Meteorology, Hamburg, Germany. [4]European Organisation for the Exploitation of Meteorological Satellites (EUMETSAT), Darmstadt, Germany. ✉e-mail: florian.roemer@uni-hamburg.de

https://doi.org/10.1038/s41561-023-01175-6

has so far largely prevented observational investigations of λ_ν. For this reason, approaches to calculate and analyse spectrally resolved long-wave feedbacks have been limited mostly to model studies[5,6,8,10–16]. Recent observational studies have demonstrated the feasibility of using hyperspectral satellite observations to derive spectral cloud radiative kernels[17] and to infer anomalies in temperature and humidity using the spectral fingerprinting method[18]. Furthermore, satellite observations have been used to calculate the spectrally resolved cloud feedback[19] and to infer both clear-sky and all-sky λ_ν over parts of the tropical ocean[20]. However, no study we are aware of has used observations to derive the global mean all-sky λ_ν, which comprises all long-wave feedbacks. To close this gap, we infer λ_ν from hyperspectral satellite observations.

One of the main challenges in deriving feedbacks from satellite observations is that the available observational time series are much shorter compared with those usually realized in model studies, making it difficult to infer λ—or even λ_ν—from long-term trends. Instead, previous studies have used short-term variability on seasonal and interannual timescales to infer λ from both models and observations[21–28]. The reasoning behind this approach is that most radiative feedbacks already occur on timescales of hours to weeks[4].

However, feedbacks derived from short-term variability are generally not the same as those derived from long-term trends[22,24–28]. These differences arise because aspects other than the global mean T_s can impact $\mathcal{L}_\nu$. Most prominently, the spatial distribution of the change in sea surface temperature is relevant because it affects overall stability and cloudiness—the so-called pattern effect (refs. 24,29 and references therein). The largest impact of the pattern effect can be seen in the short-wave cloud feedback[21–24,27,28], whereas the long-wave λ behaves similarly on short and long timescales[21,23]. However, this is not necessarily the case for the spectrally resolved λ_ν due to the potential for spectral cancellation. In fact, the long-wave cloud feedback exhibits different spectral distributions between short and long timescales[19], meaning that the long-term λ_ν might differ from the short-term λ_ν. Nevertheless, investigating how long-wave feedbacks operate on seasonal and interannual timescales—regardless of their exact relation to long-term feedbacks—gives valuable insights into the inner workings of our climate system and improves our understanding of the processes affecting long-wave feedbacks on both short and long timescales.

Therefore, we infer λ_ν from short-term variability in $\mathcal{L}_\nu$, calculated from observations by the infrared atmospheric sounding interferometer (IASI), and T_s, taken from the European Centre for Medium-Range Weather Forecasts' Reanalysis v.5 (ERA5). We perform linear regressions over both the global mean annual cycles and global monthly deviations from the mean annual cycles of both quantities to get two different estimates of λ_ν. In the following, we will refer to them as seasonal and interannual variability, respectively. Following ref. 30, we use a prediction model based on $\mathcal{L}_\nu$ simulations to extend our estimate of λ_ν to the far infrared (FIR), which is not covered by IASI. This way, we provide an observational estimate of the global mean all-sky λ_ν, covering the full spectrum of Earth's outgoing long-wave radiation.

Spectral feedbacks throughout the long-wave domain

First, we compare the observed all-sky spectral long-wave feedback parameters λ_ν with previous estimates of the all-sky long-wave feedback parameter λ by integrating spectrally. Our calculations based on seasonal and interannual variability both yield $\lambda \approx -2\ \mathrm{W\ m^{-2}\ K^{-1}}$, in agreement with previous studies (Extended Data Table 1). The observed λ_ν from seasonal and interannual variability are shown in Fig. 1; their integrals over different spectral bands are listed in Extended Data Table 2. The sensitivity of the λ_ν to the selected period, orbital drift and calibration is discussed in Supplementary Discussion 3.

For comparison, we also show the seasonal and interannual λ_ν simulated on the basis of the Max Planck Institute high-resolution

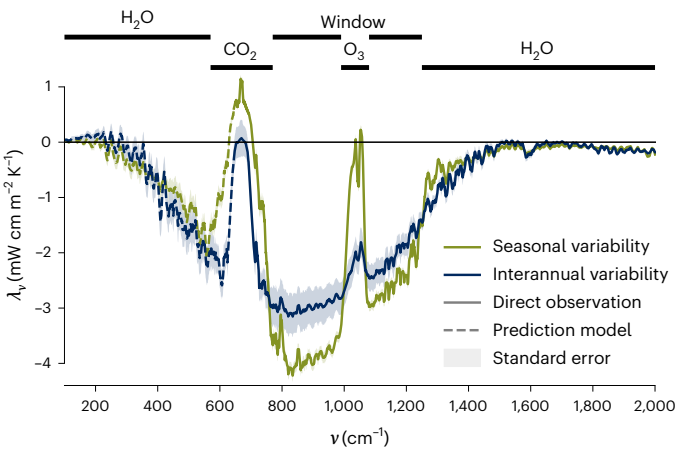


Fig. 1 | All-sky spectral long-wave feedback parameter λ_ν (10 $\mathrm{cm^{-1}}$ moving average) inferred from satellite observations by the IASI instrument. Shown are the λ_ν calculated from seasonal variability (green) and interannual variability (blue). The solid lines represent the part of the spectrum covered by IASI; the dashed lines show the λ_ν in the FIR, which are estimated using a prediction model developed by ref. 30 (Methods). Data are presented as mean value (lines) ± standard error (shading). The ranges of different spectral bands are shown at the top. For better visibility, only the spectral range 100–2,000 $\mathrm{cm^{-1}}$ is shown.

Earth system model version 1.2 (MPI-ESM1-2-HR) (Methods, Fig. 2 and Extended Data Table 3). This simulated λ_ν includes only clear-sky feedbacks because the model's horizontal resolution of about 100 km is too coarse to reliably assess the radiative impact of clouds.

In both observation and model, the largest contribution to the integrated λ comes from the atmospheric window. However, the water-vapour absorption bands in the mid-infrared (MIR) and FIR also contribute substantially. Due to their different radiative properties, the processes controlling λ_ν differ between the water-vapour bands and the atmospheric window. In the following, we separately analyse the observed λ_ν in those two spectral regions.

Stabilizing feedback in the water-vapour bands

The two water-vapour absorption bands in the MIR and FIR exhibit combined contributions to the total λ of $-0.42\ \mathrm{W\ m^{-2}\ K^{-1}}$ and $-0.47\ \mathrm{W\ m^{-2}\ K^{-1}}$ in the seasonal and interannual variability, respectively. Both all-sky λ_ν are in very good visual agreement with the findings of ref. 6, who calculated both clear-sky λ_ν (their fig. 2e) and all-sky λ_ν (their fig. 2f) on the basis of coupled climate models under forced warming. However, studies based on idealized models have found clear-sky λ_ν that are much closer to zero in the water-vapour bands[15,31].

At first, one might expect clouds to be responsible for this discrepancy. Conceptually, clouds can affect λ_ν in two different ways. First, changes in cloud fraction or cloud radiative properties can cause a cloud feedback, the net effect of which is thought to be slightly positive in the water-vapour bands[11,19]. Second, even in the absence of cloud feedbacks, clouds impact the all-sky feedback by masking part of the clear-sky feedback due to the fixed anvil temperature mechanism[32]. Both of these mechanisms indicate that clouds presumably act to dampen any negative clear-sky λ_ν. Furthermore, the negative all-sky λ_ν observed in the water-vapour bands is reproduced largely by the simulations of the clear-sky λ_ν mentioned in the preceding (Fig. 2), consistent with the findings of ref. 6. We therefore conclude that clouds are unlikely to explain the negative λ_ν observed in the water-vapour bands.

Rather, we will demonstrate in the following that the close-to-zero clear-sky λ_ν in the water-vapour bands found by idealized studies[15,31] result partly from two assumptions impacting the clear-sky physics. These assumptions pertain to the atmospheric feedback and the

https://doi.org/10.1038/s41561-023-01175-6

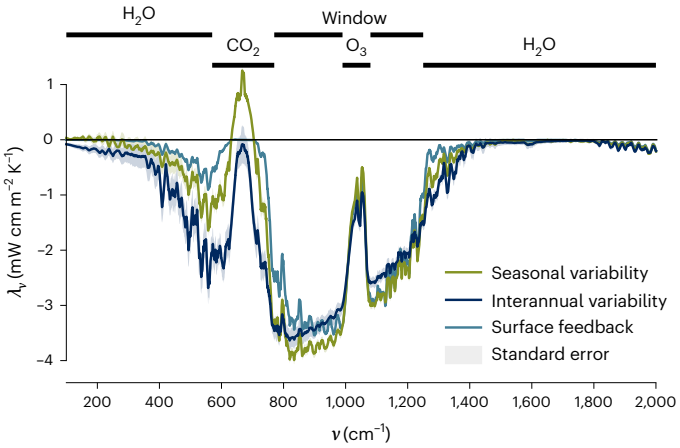


Fig. 2 | Simulated clear-sky spectral long-wave feedback parameter λ_ν (10 cm^{-1} moving average) based on the MPI-ESM1-2-HR model. Shown are the λ_ν calculated from seasonal variability (green) and interannual variability (blue), as well as the surface feedback $\lambda_{\nu,\mathrm{sfc}}$ (turquoise). Data are presented as mean value (lines) ± standard error (shading). The ranges of different spectral bands are shown at the top. For better visibility, only the spectral range 100–2,000 cm^{-1} is shown.

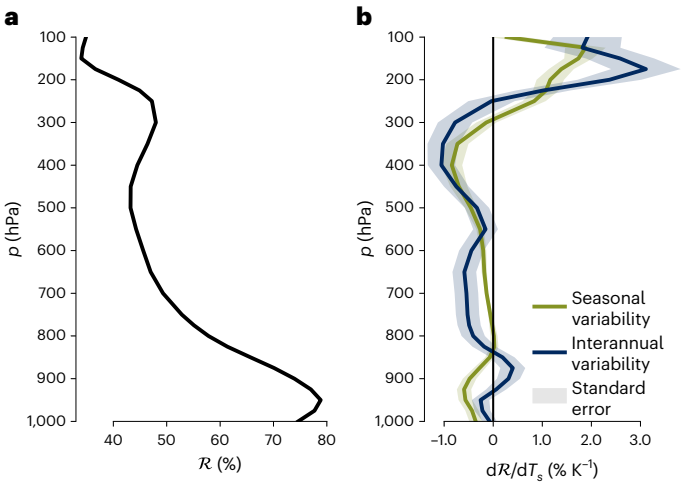


Fig. 3 | Global mean profile of relative humidity $\mathcal{R}$ and its variability in ERA5 (July 2007–March 2020). a, Global mean $\mathcal{R}$ profile (black). **b**, Change of global mean $\mathcal{R}$ with near-surface air temperature T_s due to seasonal variability (green) and interannual variability (blue). Data are presented as mean value (lines) ± standard error (shading).

surface feedback, which comprise the radiative effects of atmospheric processes and surface warming, respectively[31].

First, for the atmospheric feedback, we consider a framework first postulated by Simpson[33,34]. This framework, discussed in more depth in other studies[15,35], states that for parts of the spectrum dominated by water-vapour absorption, constant relative humidity $\mathcal{R}$ means that the specific humidity—and thus the optical depth τ—depends only on temperature. This has implications for the emission level p_{em}, the layer the spectral outgoing long-wave radiation $\mathcal{L}_\nu$ is most sensitive to, located where $\tau \approx 1$. If τ depends only on temperature, p_{em} is always located at the same temperature, causing constant $\mathcal{L}_\nu$. Applied to the feedback framework, this implies a λ_ν of close to zero. In the real world, the assumption that τ depends only on specific humidity is violated because of pressure broadening. This induces a negative feedback that is discussed in more depth in other studies[16,35,36] and accounted for in the idealized studies mentioned in the preceding[15,31].

Another assumption underlying Simpson's framework is that $\mathcal{R}$ does not change with T_s, an assumption also made by idealized studies investigating λ_ν[12–15,31]. To first order, this is a reasonable assumption: changes in $\mathcal{R}$ with T_s are generally thought to lie within ±1% K^{-1}, and this is believed to cause only a weak feedback[37–40].

To investigate how $\mathcal{R}$ varies with T_s in the analysed period, we calculate seasonal and interannual variability in $\mathcal{R}$ from the ERA5 reanalysis. In both cases, the global monthly $\mathcal{R}$ decreases with T_s between 300 hPa and 700 hPa (Fig. 3b), the layer where p_{em} in the water-vapour bands is mostly located (Extended Data Fig. 1). The change in $\mathcal{R}$ within that layer amounts to on average −0.4 ± 0.05% K^{-1} in the seasonal variability and −0.6 ± 0.09% K^{-1} in the interannual variability—in contrast to the $\mathcal{R}$ increase in the multi-decadal trend found by ref. 41.

To quantify the impact of these $\mathcal{R}$ changes, we simulate λ_ν on the basis of the one-dimensional radiative-convective equilibrium model konrad[42] (Fig. 4). We distinguish among three different scenarios: constant $\mathcal{R}$ with warming (black), decreasing $\mathcal{R}$ with T_s by −0.5% K^{-1} (brown) and increasing $\mathcal{R}$ with T_s by +0.5% K^{-1} (green). Assuming a C-shaped $\mathcal{R}$ profile (dark shading), the feedback in the water-vapour bands is −0.34 W m^{-2} K^{-1} for constant $\mathcal{R}$ with warming compared with −0.45 W m^{-2} K^{-1} for decreasing $\mathcal{R}$ and −0.23 W m^{-2} K^{-1} for increasing $\mathcal{R}$ with warming. This corresponds to a variation of ±30% in the water-vapour bands and of ±10% in the spectrally integrated λ (Extended Data Table 4). The results are similar for a vertically uniform $\mathcal{R}$ = 75%, although the effect is slightly weaker (Fig. 4, light shading). This implies that, as long as $\mathcal{R}$ is a function of temperature only, the exact shape of the $\mathcal{R}$ profile only weakly affects λ_ν in the water-vapour bands, in agreement with existing studies[33–35]. Because we perform the simulations under clear-sky conditions and assume that $\mathcal{R}$ variations are vertically uniform, these numbers might be a slight overestimate. Nevertheless, these results show that even small changes in $\mathcal{R}$ with T_s represent a first-order effect for both the spectral λ_ν and the broadband λ.

Second, we calculate the surface feedback, the change in $\mathcal{L}_\nu$ caused by surface warming alone, on the basis of the MPI-ESM1-2-HR model (turquoise line in Fig. 2; Extended Data Table 3 and Methods). Integrated over both water-vapour bands, the surface feedback amounts to −0.13 W m^{-2} K^{-1}, while it is zero in ref. 15 (their fig. 2f). However, their single-column set-up by design does not account for horizontal variations in temperature and thus absolute humidity. To demonstrate the effect of these variations, we simulate the surface feedback for different T_s using konrad (Fig. 5 and Methods). For the simulations, we assume the same C-shaped $\mathcal{R}$ profile mentioned in the preceding for all T_s, and thus exponentially increasing integrated water vapour $\mathcal{W}$ (Methods). While the surface feedback in the water-vapour bands is zero for the moist atmospheres with T_s at or above the global mean (purple lines), it is strongly negative for the dry atmospheres at low T_s (blue lines). This causes the mean surface feedback to also be negative (black line)—analogous to the concept of 'radiator fins'[43,44].

As mentioned, the λ_ν values derived from IASI observations for the FIR are based on a prediction model introduced by Turner et al.[30]. Future missions such as the Far-infrared Outgoing Radiation Understanding and Monitoring (FORUM) and the Polar Radiant Energy in the Far Infrared Experiment (PREFIRE) will provide spectrally resolved observations of the entire FIR. These observations will also provide a test of the method presented here, shedding light on how well the λ_ν in the MIR water-vapour band is suited as a proxy for the λ_ν in the FIR. In contrast to the MIR, substantial parts of the FIR are sensitive to the layer above 300 hPa, and the parts of the FIR that are sensitive to layers below 500 hPa do not exhibit absorption by methane.

Surface feedback variations in the atmospheric window

In the atmospheric window, our interannual λ_ν is in good visual agreement with modelling studies of both clear-sky and all-sky λ_ν, whereas our seasonal λ_ν is 0.26 W m^{-2} K^{-1} more negative (fig. 2f in ref. 6; fig. 7 (bottom)

https://doi.org/10.1038/s41561-023-01175-6

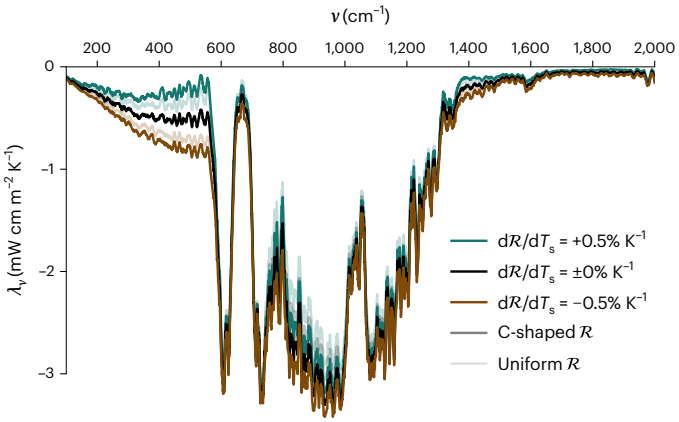


Fig. 4 | Simulated clear-sky spectral long-wave feedback parameter λ_ν (10 cm^{-1} moving average) based on simulations using konrad[42]. Shown are the λ_ν for constant $\mathcal{R}$ with warming (black) and for changes of $\mathcal{R}$ with T_s of −0.5% K^{-1} (brown) and +0.5% K^{-1} (green). For all three cases, we separately show the λ_ν for the C-shaped global mean $\mathcal{R}$ profile shown in Fig. 3a (dark shading) and for a vertically uniform $\mathcal{R}$ = 75% (light shading). For better visibility, only the spectral range 100–2,000 cm^{-1} is shown.

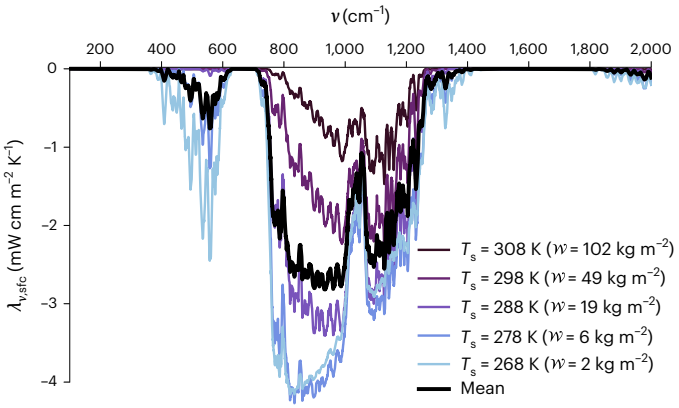


Fig. 5 | Simulated clear-sky spectral surface feedback $\lambda_{\nu,sfc}$ based on simulations using konrad for different near-surface air temperatures T_s. For each T_s, the integrated water vapour $\mathcal{W}$ is given. The surface feedback averaged over all five different T_s is also shown (thick black line). For better visibility, only the spectral range 100–2,000 cm^{-1} is shown.

in ref. 12; fig. 2f in ref. 15). To explain this difference between seasonal and interannual variability, we first consider the surface feedback, which is the dominating factor impacting λ_ν in the window (turquoise line in Fig. 2; Extended Data Table 3). Conceptually, the strength of the surface feedback depends on two factors: (1) how much surface emission varies with near-surface air temperature T_s and (2) how much of that surface emission is absorbed by the atmosphere.

First, the variability of surface emission with T_s to first order depends on how much the skin temperature T_{skin}, the temperature of the ocean or land surface, varies with T_s. In ERA5, the global mean T_{skin} changes about 6% more strongly with global mean T_s in the seasonal variability (1.03 ± 0.004 K K^{-1}) compared with the interannual variability (0.97 ± 0.012 K K^{-1}). Approximating the Planck curve as linear, this stronger variability in T_{skin} would explain a difference in λ_ν in the window of about 0.06 W m^{-2} K^{-1}.

Second, the atmospheric absorption of surface emission in the window is caused mainly by water vapour. Therefore, the surface feedback in the window is stronger for dry atmospheres compared with moist atmospheres (Fig. 5). When we compare the spatial patterns of seasonal and interannual variability in the local skin temperature T^*_{skin} with global T_s, we find that the seasonal variability in T^*_{skin} originates mostly from the continents of the Northern Hemisphere, particularly at high latitudes, whereas the interannual variability is also substantial in the tropics (Fig. 6). Hence, the seasonal variability occurs under drier atmospheres on average, which causes a stronger surface feedback and thus a more negative seasonal λ_ν.

Apart from the clear-sky processes discussed in the preceding, clouds also play an important role in the atmospheric window. The simulated clear-sky λ_ν from seasonal and interannual variability differ by only about 0.1 W m^{-2} K^{-1}—much less than the observed all-sky λ_ν (Fig. 2 and Extended Data Table 3). Furthermore, according to ref. 19, the cloud feedback in the window is about 0.1 W m^{-2} K^{-1} in the short term but about 25% weaker in the long term. Therefore, it seems plausible that the cloud feedback also differs between seasonal and interannual timescales, explaining some of the observed difference in λ_ν.

Spectral observations can constrain climate sensitivity

We infer the spectral long-wave feedback parameter λ_ν from satellite observations of seasonal and interannual variability. This way, we

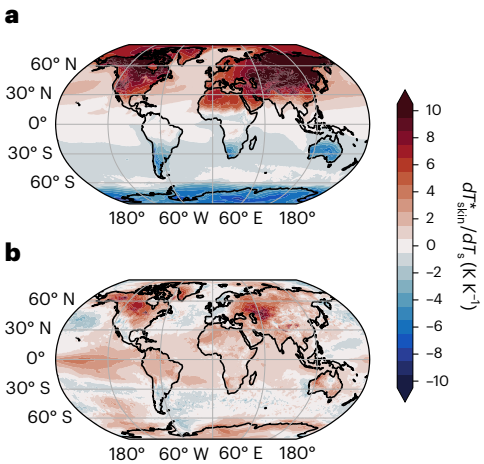


Fig. 6 | Change in local skin temperature T^*_{skin} with global mean near-surface air temperature T_s in ERA5 (July 2007–March 2020). a,**b**, The changes of T^*_{skin} in seasonal variability (**a**) and interannual variability (**b**).

demonstrate that the spectral fingerprint of the net long-wave feedback can be directly observed using hyperspectral satellite instruments such as IASI. Furthermore, we use a prediction model to extend the spectra observed by IASI to the FIR. In the future, analogous models could be used to calculate λ_ν from other infrared sounders that have gaps in their spectral coverage, such as the atmospheric infrared sounder (AIRS) and the cross-track infrared sounder (CsIR).

When integrating λ_ν spectrally, we find a long-wave feedback parameter $\lambda \approx -2$ W m^{-2} K^{-1}, in agreement with the existing body of evidence. When spectrally integrating over the water-vapour absorption bands alone, we find a considerably negative feedback of almost −0.5 W m^{-2} K^{-1}. This negative λ_ν results partly from the change of relative humidity $\mathcal{R}$ with warming. Because direct observations of λ_ν contain the radiative fingerprint of this $\mathcal{R}$ change, they can provide a more realistic picture of λ_ν compared with idealized model studies.

Our findings emphasise the importance of better understanding processes affecting the present distribution and the future trends of $\mathcal{R}$. Despite recent progress in this field, due partly to the development of global storm-resolving models (GSRMs), substantial uncertainties

remain[45]. By providing an observational constraint on λ_v, our results can be used to evaluate whether GSRMs correctly represent long-wave feedbacks—and thus by extension variability in $\mathcal{R}$—on seasonal and interannual timescales. Due to the high spatial resolution of GSRMs, comparable to observations, this evaluation can also include the effect of clouds. This can put powerful constraints on the processes that also govern the long-term long-wave feedback and thus Earth's climate sensitivity.

Online content

Any methods, additional references, Nature Portfolio reporting summaries, source data, extended data, supplementary information, acknowledgements, peer review information; details of author contributions and competing interests; and statements of data and code availability are available at https://doi.org/10.1038/s41561-023-01175-6.

References

1. Hansen, J. & Takahashi, T. (eds) in *Climate Processes and Climate Sensitivity* 130–163 (AGU, 1984).
2. Gregory, J. M. et al. A new method for diagnosing radiative forcing and climate sensitivity. *Geophys. Res. Lett.* **31**, L03205 (2004).
3. Soden, B. J. et al. Quantifying climate feedbacks using radiative kernels. *J. Clim.* **21**, 3504–3520 (2008).
4. Sherwood, S. C. et al. An assessment of Earth's climate sensitivity using multiple lines of evidence. *Rev. Geophys.* **58**, e2019RG000678 (2020).
5. Slingo, A. & Webb, M. J. The spectral signature of global warming. *Q. J. R. Meteorol. Soc.* **123**, 293–307 (1997).
6. Huang, X., Chen, X., Soden, B. J. & Liu, X. The spectral dimension of longwave feedback in the CMIP3 and CMIP5 experiments. *Geophys. Res. Lett.* **41**, 7830–7837 (2014).
7. Brindley, H. & Bantges, R. The spectral signature of recent climate change. *Curr. Clim. Change Rep.* **2**, 112–126 (2016).
8. Pan, F. & Huang, X. The spectral dimension of modeled relative humidity feedbacks in the CMIP5 experiments. *J. Clim.* **31**, 10021–10038 (2018).
9. Madden, R. A. & Ramanathan, V. Detecting climate change due to increasing carbon dioxide. *Science* **209**, 763–768 (1980).
10. Leroy, S., Anderson, J., Dykema, J. & Goody, R. Testing climate models using thermal infrared spectra. *J. Clim.* **21**, 1863–1875 (2008).
11. Huang, Y., Leroy, S., Gero, P. J., Dykema, J. & Anderson, J. Separation of longwave climate feedbacks from spectral observations. *J. Geophys. Res. Atmos.* **115**, D07104 (2010).
12. Kluft, L., Dacie, S., Buehler, S. A., Schmidt, H. & Stevens, B. Re-examining the first climate models: climate sensitivity of a modern radiative-convective equilibrium model. *J. Clim.* **32**, 8111–8125 (2019).
13. Kluft, L., Dacie, S., Brath, M., Buehler, S. A. & Stevens, B. Temperature-dependence of the clearsky feedback in radiative-convective equilibrium. *Geophys. Res. Lett.* **48**, e2021GL094649 (2021).
14. Seeley, J. T. & Jeevanjee, N. H_2O windows and CO_2 radiator fins: a clear-sky explanation for the peak in equilibrium climate sensitivity. *Geophys. Res. Lett.* **48**, e2020GL089609 (2021).
15. Jeevanjee, N., Koll, D. D. B. & Lutsko, N. "Simpson's law" and the spectral cancellation of climate feedbacks. *Geophys. Res. Lett.* **48**, e2021GL093699 (2021).
16. Koll, D. D., Jeevanjee, N. & Lutsko, N. J. An analytical model for the clear-sky longwave feedback. Preprint at *Authorea* https://doi.org/10.1002/essoar.10512192.1 (2022).
17. Yue, Q. et al. Observation-based longwave cloud radiative kernels derived from the A-Train. *J. Clim.* **29**, 2023–2040 (2016).
18. Wu, W., Liu, X., Yang, Q., Zhou, D. K. & Larar, A. M. Radiometrically consistent climate fingerprinting using CrIS and AIRS hyperspectral observations. *Remote Sens.* **12**, 1291 (2020).
19. Huang, X., Chen, X. & Yue, Q. Band-by-band contributions to the longwave cloud radiative feedbacks. *Geophys. Res. Lett.* **46**, 6998–7006 (2019).
20. Huang, Y. & Ramaswamy, V. Observed and simulated seasonal co-variations of outgoing longwave radiation spectrum and surface temperature. *Geophys. Res. Lett.* **35**, L17803 (2008).
21. Zhou, C., Zelinka, M. D., Dessler, A. E. & Klein, S. A. The relationship between interannual and long-term cloud feedbacks. *Geophys. Res. Lett.* **42**, 10463–10469 (2015).
22. Zhou, C., Zelinka, M. D. & Klein, S. A. Impact of decadal cloud variations on the Earth's energy budget. *Nat. Geosci.* **9**, 871–874 (2016).
23. Colman, R. & Hanson, L. On the relative strength of radiative feedbacks under climate variability and change. *Clim. Dyn.* **49**, 2115–2129 (2017).
24. Dong, Y. et al. Intermodel spread in the pattern effect and its contribution to climate sensitivity in CMIP5 and CMIP6 models. *J. Clim.* **33**, 7755–7775 (2020).
25. Dessler, A. E. Observations of climate feedbacks over 2000–10 and comparisons to climate models. *J. Clim.* **26**, 333–342 (2013).
26. Dessler, A. E. & Forster, P. M. An estimate of equilibrium climate sensitivity from interannual variability. *J. Geophys. Res. Atmos.* **123**, 8634–8645 (2018).
27. Andrews, T., Gregory, J. M. & Webb, M. J. The dependence of radiative forcing and feedback on evolving patterns of surface temperature change in climate models. *J. Clim.* **28**, 1630–1648 (2015).
28. Dessler, A. E. Potential problems measuring climate sensitivity from the historical record. *J. Clim.* **33**, 2237–2248 (2020).
29. Ceppi, P., Brient, F., Zelinka, M. D. & Hartmann, D. L. Cloud feedback mechanisms and their representation in global climate models. *Wiley Interdiscip. Rev. Clim. Change* **8**, e465 (2017).
30. Turner, E. C., Lee, H.-T. & Tett, S. F. B. Using IASI to simulate the total spectrum of outgoing long-wave radiances. *Atmos. Chem. Phys.* **15**, 6561–6575 (2015).
31. Koll, D. D. B. & Cronin, T. W. Earth's outgoing longwave radiation linear due to H_2O greenhouse effect. *Proc. Natl Acad. Sci. USA* **115**, 10293–10298 (2018).
32. Hartmann, D. L. & Larson, K. An important constraint on tropical cloud–climate feedback. *Geophys. Res. Lett.* **29**, 1951 (2002).
33. Simpson, G. Some studies in terrestrial radiation. *Mem. R. Meteorol. Soc.* **2**, 69–95 (1928).
34. Simpson, G. Further studies in terrestrial radiation. *Mem. R. Meteorol. Soc.* **3**, 1–26 (1928).
35. Ingram, W. A very simple model for the water vapour feedback on climate change. *Q. J. R. Meteorol. Soc.* **136**, 30–40 (2010).
36. Feng, J., Paynter, D. & Menzel, R. How a stable greenhouse effect on Earth is maintained under global warming. Preprint at *Authorea* https://doi.org/10.1002/essoar.10512049.1 (2022).
37. Sherwood, S. C. et al. Relative humidity changes in a warmer climate. *J. Geophys. Res. Atmos.* **115**, D09104 (2010).
38. Held, I. M. & Shell, K. M. Using relative humidity as a state variable in climate feedback analysis. *J. Clim.* **25**, 2578–2582 (2012).
39. Jeevanjee, N. The physics of climate change: simple models in climate science. *arXiv* https://doi.org/10.48550/arXiv.1802.02695 (2018).
40. Zelinka, M. D. et al. Causes of higher climate sensitivity in CMIP6 models. *Geophys. Res. Lett.* **47**, e2019GL085782 (2020).
41. Bourdin, S., Kluft, L. & Stevens, B. Dependence of climate sensitivity on the given distribution of relative humidity. *Geophys. Res. Lett.* **48**, e2021GL092462 (2021).

42. Kluft, L. & Dacie, S. atmtools/konrad: A radiative-convective equilibrium model for Python v.1.0.1 (2022).
43. McKim, B. A., Jeevanjee, N. & Vallis, G. K. Joint dependence of longwave feedback on surface temperature and relative humidity. *Geophys. Res. Lett.* **48**, e2021GL094074 (2021).
44. Pierrehumbert, R. T. Thermostats, radiator fins, and the local runaway greenhouse. *J. Atmos. Sci.* **52**, 1784–1806 (1995).
45. Lang, T., Naumann, A. K., Stevens, B. & Buehler, S. A. Tropical free-tropospheric humidity differences and their effect on the clear-sky radiation budget in global storm-resolving models. *J. Adv. Model. Earth Syst.* **13**, e2021MS002514 (2021).

Publisher's note Springer Nature remains neutral with regard to jurisdictional claims in published maps and institutional affiliations.

Open Access This article is licensed under a Creative Commons Attribution 4.0 International License, which permits use, sharing, adaptation, distribution and reproduction in any medium or format, as long as you give appropriate credit to the original author(s) and the source, provide a link to the Creative Commons license, and indicate if changes were made. The images or other third party material in this article are included in the article's Creative Commons license, unless indicated otherwise in a credit line to the material. If material is not included in the article's Creative Commons license and your intended use is not permitted by statutory regulation or exceeds the permitted use, you will need to obtain permission directly from the copyright holder. To view a copy of this license, visit http://creativecommons.org/licenses/by/4.0/.

© The Author(s) 2023

Methods

Data

IASI provides hyperspectral measurements of outgoing spectral radiances in 8,461 channels in the thermal infrared (645–2,760 cm^{-1}) with a spectral sampling of 0.25 cm^{-1} and a spectral resolution after apodization of 0.5 cm^{-1}. IASI scans across track, with 30 different elementary fields of view symmetrically spanning ±48.33° relative to nadir. This corresponds to a maximum satellite zenith angle θ_{max} as seen from Earth of about ±59°. Each elementary field of view is sampled by a 2 × 2 array of circular instantaneous fields of view (IFOVs). The highest horizontal resolution is reached directly below the satellite, with an IFOV diameter of 12 km. The swath width on ground is about 2,200 km, causing the IFOV diameter to increase to 20 × 39 km at swath edge[46,47]. We use the IASI level 1c (L1C) data from the meteorological operational satellite (Metop) A from July /2007 to December 2016[48] and operational IASI level 1c data from Metop A from January 2017 to March 2020.

For the full period (July 2007–March 2020), we use the Clouds and the Earth's Radiant Energy System CERES EBAF-TOA–Level 3b dataset for comparison[49].

Atmospheric variables are taken from the ERA5. This includes hourly fields of 2 m air temperature and skin temperature[50] as well as hourly profiles of relative humidity[51–59]. We use ERA5's global mean monthly 2 m air temperature to calculate λ_v as it is a very robust variable constantly validated against observations[60]. Hence, we are confident that any errors in T_s have a negligible effect on our estimates of λ_v. Furthermore, ERA5's temperature and humidity profiles, as well as its skin temperature, are used for the analysis of the underlying feedback processes.

To simulate the model-based clear-sky λ_v, we use model output of the MPI-ESM1-2-HR Earth system model[61] prepared for the 'historical' experiment of the sixth phase of the Coupled Model Intercomparison Project[62]. For the simulated years 2000–2014, the used data include daily profiles of atmospheric temperature and specific humidity on 95 vertical levels, near-surface values of air temperature, specific humidity, air pressure and horizontal wind components, as well as skin temperature, surface type, surface elevation and sea-ice concentration[63].

Spectral outgoing long-wave radiation from observations

The spectral long-wave feedback parameter λ_v is defined in equation (1) in terms of spectral outgoing long-wave radiation $\mathcal{L}_v$, a spectral flux. However, IASI measures outgoing spectral radiances $I_v(\theta)$ for different satellite zenith angles θ as seen from Earth. Hence, the $I_v(\theta)$ need to be integrated over all θ to yield the desired $\mathcal{L}_v$. However, some intermediary steps are necessary before we proceed to this angular integration.

First, we account for the fact that high latitudes are oversampled by IASI due to Metop's polar-orbiting track. We sort all observed $I_v(\theta, l)$ into 1° latitude bins l centred at latitude l_c, whose area is proportional to $\cos(l_c)$. Relating this area to the actual number of observed $I_v(\theta, l)$ within that bin, $N(l)$, yields the correction factor

$$\alpha(l) = \frac{\cos(l_c)}{N(l)}, \tag{2}$$

which we estimate by averaging over 40 orbits.

Second, we use $\alpha(l)$ as weights to average over all $M(\theta)$ spectra in each orbit b that are observed under the same θ. Thereby, we assume azimuthal symmetry to aggregate the left and right sides of the swath. This yields the spectral radiance averaged over orbit b for 15 different zenith angles θ as

$$\overline{I_{v,b}}(\theta) = \frac{1}{A_b}\sum_{i=1}^{M(\theta)} I_{v,i}(\theta, l)\,\alpha_i(l), \tag{3}$$

$$A_b = \sum_{i=1}^{M(\theta)} \alpha_i(l), \tag{4}$$

$$\theta \in [0°, \theta_{max}]. \tag{5}$$

where $\theta_{max} \approx 59°$ is the maximum θ under which spectra are observed by IASI.

Third, we need to account for the fact there are no IASI observations of $I_v(\theta)$ for $\theta > \theta_{max}$. Hence, we perform a linear interpolation between θ_{max} and 90° of $\overline{I_{v,b}}(\theta)\cos(\theta)$, which is zero for $\theta = 90°$, to calculate $\overline{I_{v,b}}(\theta)$ for those angles as

$$\begin{aligned}\overline{I_{v,b}}(\theta)\cos(\theta) &= \overline{I_{v,b}}(\theta_{max})\cos(\theta_{max}) \\ &+ \left(\overline{I_{v,b}}(90°)\ \cos(90°) - \overline{I_{v,b}}(\theta_{max})\ \cos(\theta_{max})\right)\frac{\theta-\theta_{max}}{90°-\theta_{max}},\end{aligned} \tag{6}$$

$$\overline{I_{v,b}}(\theta)\cos(\theta) = \overline{I_{v,b}}(\theta_{max})\ \cos(\theta_{max})\left(1 - \frac{\theta-\theta_{max}}{90°-\theta_{max}}\right), \tag{7}$$

$$\theta \in]\theta_{max}, 90°]. \tag{8}$$

For each orbit separately, we calculate the mean $\mathcal{L}_{v,b}$ by conducting an angular integration over the $\overline{I_{v,b}}(\theta)$ calculated in equations (3)–(8), respectively. Assuming azimuthal symmetry, this yields

$$\mathcal{L}_{v,b} = 2\pi \int_{\theta=0°}^{90°} \overline{I_{v,b}}(\theta)\ \cos(\theta)\ \sin(\theta)\,\mathrm{d}\theta. \tag{9}$$

Finally, we calculate the monthly mean $\mathcal{L}_v$ by averaging over all orbits in the respective month as

$$\mathcal{L}_v = \frac{\sum_b L_{v,b} A_b}{\sum_b A_b}. \tag{10}$$

The spectral integral of this monthly mean $\mathcal{L}_v$ is compared with CERES observations in Supplementary Discussion 2 and Supplementary Fig. 2.

Spectral outgoing long-wave radiation from model

We use the Radiative Transfer for TOVS (RTTOV) model version 12.2[64] to simulate outgoing spectral radiances I_v in all 8,461 IASI channels between 645 cm^{-1} and 2,760 cm^{-1} with a spectral sampling of 0.25 cm^{-1}. In addition, we simulate I_v in 1,817 channels of the planned Far-infrared Outgoing Radiation Understanding and Monitoring mission[65] between 100 cm^{-1} and 645 cm^{-1} with a spectral sampling of 0.3 cm^{-1}. As input for the radiative transfer simulations, we use the MPI-ESM1-2-HR model output described in the preceding. The profiles of temperature and humidity, which represent the mean over the respective vertical layer, are interpolated in log pressure to the layer bounds, as required by RTTOV. We perform clear-sky simulations only by setting the cloud liquid and cloud ice contents to zero. For ozone, we use RTTOV's internal climatology[66]. We conduct those radiative transfer simulations for 500 randomly selected profiles per day.

For every selected profile, we calculate outgoing radiances $I_v(\theta)$ in all 10,278 channels for two different satellite zenith angles $(\theta_1, \theta_2) = (37.9°, 77.8°)$. We then apply a two-angle Gauss–Legendre quadrature[67] to approximate $\mathcal{L}_v$ as

$$\mathcal{L}_v \approx 2\pi \sum_{i=1}^{2} I_v(\mu_i)\mu_i\, w_i, \tag{11}$$

where $\mu_i = \cos(\theta_i)$ and the weights $w_i = 0.5$. RTTOV supports simulations only for $\theta \le 75°$, so we infer $I_v(\theta_2)$ by interpolating between 75° and 90°, analogous to equations (6)–(8). The $\mathcal{L}_v$ spectra are averaged monthly.

Prediction model for FIR

The spectral range covered by IASI does not include the FIR, which contributes substantially to the total outgoing long-wave radiation $\mathcal{L}$. Hence, we extend our calculation of the observed all-sky $\mathcal{L}_v$ to the FIR. The different steps are described in the following.

The simulated monthly clear-sky $\mathcal{L}_\nu$ spectra are used to set up a prediction model, closely following ref. 30. For every channel between 100 cm^{-1} and 645 cm^{-1}, we calculate the correlation coefficient of $\ln(\mathcal{L}_\nu)$ with every IASI channel from 645 cm^{-1} to 2,760 cm^{-1}. Then the IASI channel with the highest correlation is selected as predictor channel for the respective channel between 100 cm^{-1} and 645 cm^{-1}. The $\mathcal{L}_\nu$ of these channels are then calculated analogous to equation (1) in ref. 30 as

$$\ln\left(\mathcal{L}_{\nu,\mathrm{FIR}}\right) = \alpha_0 + \alpha_1 \ln\left(\mathcal{L}_{\nu,\mathrm{predictor}}\right), \tag{12}$$

where $\mathcal{L}_{\nu,\mathrm{predictor}}$ are the monthly mean IASI observations and α_0 and α_1 are the regression coefficients.

Calculation of spectral long-wave feedback parameter

We use both the simulated clear-sky $\mathcal{L}_\nu$ spectra and the extended observational all-sky $\mathcal{L}_\nu$ spectra to calculate λ_ν from both seasonal and interannual variability, respectively. To this end, we perform linear ordinary least-squares regressions of monthly means, with $\mathcal{L}_\nu$ as dependent variable and T_s as independent variable, and subtract the means over the whole period, yielding monthly anomalies of $\mathcal{L}_\nu$ and T_s.

To calculate λ_ν from seasonal variability, we then calculate the mean annual cycles of those monthly anomalies in both $\mathcal{L}_\nu$ and T_s (Supplementary Fig. 1b). We then regress the mean annual cycle in $\mathcal{L}_\nu$ against the mean annual cycle of T_s. The slope of the regression delivers an estimate of λ_ν from seasonal variability (Supplementary Fig. 1c).

To calculate λ_ν from interannual variability, we subtract these mean annual cycles of $\mathcal{L}_\nu$ and T_s from the respective time series of monthly anomalies, yielding the deviations from the mean annual cycles for every single month. Assuming that the radiative forcing changes linearly over the analysed period, we calculate the linear trend in those deviations using an ordinary least-squares regression and then subtract that trend from the time series as well, following ref. 26. The detrended deviations from the mean annual cycle in $\mathcal{L}_\nu$ (Supplementary Fig. 1d) are then regressed against the deviations in T_s to infer λ_ν from interannual variability (Supplementary Fig. 1e).

Calculation of atmospheric variability

We use the same methodology as for the feedback calculation described in the preceding to calculate seasonal and interannual variability with T_s for the global mean profile of relative humidity $\mathcal{R}$, as well as for both the global mean and spatially resolved skin temperature T_skin. All calculations are performed for monthly mean values.

Calculation of surface feedback

We use the same radiative transfer simulations described in the preceding to calculate global mean values of an idealized surface feedback. In those simulations, we calculate $t_{\nu,\theta_i}(p, \mathrm{TOA})$, the transmittance of the simulated spectral radiances $I_\nu(\theta_i)$ from every input pressure level p to the top of the atmosphere (TOA), from which we then approximate $t_\nu(p, \mathrm{TOA})$, the transmittance with respect to $\mathcal{L}_\nu$, as

$$t_\nu(p, \mathrm{TOA}) \approx \sum_{i=1}^{2} t_{\nu,\theta_i}(p, \mathrm{TOA}) \cos(\theta_i). \tag{13}$$

We use $t_\nu(\mathrm{sfc}, \mathrm{TOA})$, the transmittance from the surface to TOA, to calculate an idealized estimate of the spectral long-wave surface feedback as

$$\lambda_{\nu,\mathrm{sfc}} \approx t_\nu(\mathrm{sfc}, \mathrm{TOA})\pi \left.\frac{\mathrm{d}B_\nu}{\mathrm{d}T}\right|_{T=288\,\mathrm{K}} \tag{14}$$

Conceptually, the surface feedback represents the radiative signature of surface warming at TOA. This signature consists of (1) the additional radiation emitted by the surface per 1 K of warming, estimated by the derivative of the Planck function B_ν with temperature T at the global mean T_s of 288 K, multiplied by π to convert to a spectral flux, and (2) the fraction of this additional surface emission that reaches TOA, estimated by $t_\nu(\mathrm{sfc}, \mathrm{TOA})$, the global mean transmittance of the whole atmospheric column for each spectral channel. The T_s dependence of $\lambda_{\nu,\mathrm{sfc}}$ is derived from the single-column simulations discussed in the following.

Calculation of emission level

From the $t_\nu(\mathrm{sfc}, \mathrm{TOA})$, we calculate the optical depth with respect to $\mathcal{L}_\nu$ as

$$\tau_\nu(p, \mathrm{TOA}) = -\ln\left(t_\nu(p, \mathrm{TOA})\right), \tag{15}$$

from which we calculate the emission level with respect to $\mathcal{L}_\nu$ as

$$p_{\mathrm{em},\nu} = \max\left(p\left[\tau_\nu(p, \mathrm{TOA}) \le 1\right]\right). \tag{16}$$

Idealized single-column simulations

We use the single-column model konrad v.1.0.1[42], developed by Kluft et al.[12] and Dacie et al.[68], which provides an idealized representation of the clear-sky tropical atmosphere assuming radiative-convective equilibrium. We calculate $\mathcal{L}_\nu$ for a 'cool' profile with T_s = 288 K and a 'warm' profile with T_s = 289 K. We then calculate λ_ν as the difference between the warm $\mathcal{L}_\nu$ and the cool $\mathcal{L}_\nu$. The $\mathcal{L}_\nu$ are calculated using the line-by-line radiative transfer model ARTS[69,70] in the same spectral range used in the preceding (100–2,760 cm^{-1}) with a spectral resolution of about 0.1 cm^{-1}.

To quantify the impact of changes in $\mathcal{R}$ with T_s on λ_ν, we perform six different experiments. In three of them, we use a C-shaped $\mathcal{R}$ distribution (Fig. 3a); in the other three experiments, we assume a vertically uniform $\mathcal{R}$ = 75%. To predict changes of $\mathcal{R}$ with surface warming, we use T as a vertical coordinate, following ref. 71. For both mean $\mathcal{R}$ distributions, we consider three different cases. In the first case, we keep $\mathcal{R}(T)$ constant with increasing T_s. In the second and third cases, we let $\mathrm{d}\mathcal{R}(T)/\mathrm{d}T_\mathrm{s} = -0.5\%\,\mathrm{K}^{-1}$ and $\mathrm{d}\mathcal{R}(T)/\mathrm{d}T_\mathrm{s} = +0.5\%\,\mathrm{K}^{-1}$ throughout the atmospheric column, respectively. For each of the six experiments, we calculate λ_ν as described in the preceding.

We also use konrad to investigate the temperature dependence of the surface feedback. To this end, we calculate $\mathcal{L}_\nu$ for five different T_s between 268 K and 308 K in 10 K increments. For the calculations, we again use a C-shaped $\mathcal{R}$ distribution (Fig. 3a). In contrast to the preceding, we derive the surface feedback by increasing T_s by 1 K, but not adjusting the atmospheric profiles of temperature and humidity, which isolates the radiative effects of surface warming. For reference, we also calculate the integrated water vapour of those profiles as

$$\mathcal{W} = -\frac{1}{g}\int q(p)\,\mathrm{d}p, \tag{17}$$

where q is the specific humidity and g is the gravitational acceleration.

Data availability

The processed data used to derive the main results of this study are available at https://doi.org/10.26050/WDCC/FluxFeedb_ObsSim_v2 (ref. 72). This includes global monthly averages of the spectrally resolved outgoing long-wave radiation derived from IASI observations and calculated on the basis of both the MPI-ESM1-2-HR and konrad models. Furthermore, IASI Level 1C Climate Data Record Release 1 - Metop-A (10.15770/EUM_SEC_CLM_0014) can be ordered through the EUMETSAT User Helpdesk (https://www.eumetsat.int/contact-us). The operational IASI L1c data can be directly downloaded from the EUMETSAT Data Store (https://data.eumetsat.int/data/map/EO:EUM:DAT:METOP:IASIL1C-ALL#). The ERA5 reanalysis data can be downloaded from the Copernicus Climate Change Service (C3S) Climate Data Store for the data on pressure levels (https://doi.org/10.24381/cds.bd0915c6) and single levels (https://doi.org/10.24381/cds.adbb2d47).

The MPI-ESM1-2-HR model output prepared for CMIP6 can be downloaded from https://esgf-data.dkrz.de/search/cmip6-dkrz. The CERES EBAF Ed4.0 dataset can be downloaded from https://ceres.larc.nasa.gov/data. Source data are provided with this paper.

Code availability

The computer code used to produce the central results of this study is available upon request from the corresponding author.

References

46. August, T. et al. IASI on Metop-A: operational Level 2 retrievals after five years in orbit. *J. Quant. Spectrosc. Radiat. Transf.* **113**, 1340–1371 (2012).
47. Blumstein, D. et al. IASI instrument: technical overview and measured performances. *Proc. SPIE - The Inter. Soc. for Opt. Engineering* **5543**, 196–207 (2004).
48. *IASI Level 1C Climate Data Record Release 1—Metop-A* (EUMETSAT, 2018).
49. Loeb, N. G. et al. Clouds and the Earth's Radiant Energy System (CERES) Energy Balanced and Filled (EBAF) Top-of-Atmosphere (TOA) edition-4.0 data product. *J. Clim.* **31**, 895–918 (2018).
50. Hersbach, H. et al. *ERA5 Hourly Data on Single Levels from 1979 to Present* (Copernicus Climate Change Service, accessed 26 November 2021).
51. Hersbach, H. et al. *ERA5 Hourly Data on Pressure Levels from 1979 to Present* (Copernicus Climate Change Service, accessed 27 January 2022).
52. Chung, E.-S., Yeomans, D. & Soden, B. An assessment of climate feedback processes using satellite observations of clear-sky OLR. *Geophys. Res. Lett.* **37**, L02702 (2010).
53. Budyko, M. I. The effect of solar radiation variations on the climate of the Earth. *Tellus* **21**, 611–619 (1969).
54. Forster, P. M. F. & Gregory, J. M. The climate sensitivity and its components diagnosed from Earth radiation budget data. *J. Clim.* **19**, 39–52 (2006).
55. Murphy, D. M. et al. An observationally based energy balance for the Earth since 1950. *J. Geophys. Res. Atmos.* **114**, D17107 (2009).
56. Donohoe, A., Armour, K. C., Pendergrass, A. G. & Battisti, D. S. Shortwave and longwave radiative contributions to global warming under increasing CO_2. *Proc. Natl Acad. Sci. USA* **111**, 16700–16705 (2014).
57. Trenberth, K. E., Zhang, Y., Fasullo, J. T. & Taguchi, S. Climate variability and relationships between top-of-atmosphere radiation and temperatures on Earth. *J. Geophys. Res. Atmos.* **120**, 3642–3659 (2015).
58. Tsushima, Y., Abe-Ouchi, A. & Manabe, S. Radiative damping of annual variation in global mean surface temperature: comparison between observed and simulated feedback. *Clim. Dyn.* **24**, 591–597 (2005).
59. Tsushima, Y. & Manabe, S. Assessment of radiative feedback in climate models using satellite observations of annual flux variation. *Proc. Natl Acad. Sci. USA* **110**, 7568–7573 (2013).
60. Hersbach, H. et al. The ERA5 global reanalysis. *Q. J. R. Meteorol. Soc.* **146**, 1999–2049 (2020).
61. Müller, W. A. et al. A higher-resolution version of the Max Planck Institute Earth system model (MPI-ESM1.2-HR). *J. Adv. Model. Earth Syst.* **10**, 1383–1413 (2018).
62. Eyring, V. et al. Overview of the Coupled Model Intercomparison Project Phase 6 (CMIP6) experimental design and organization. *Geosci. Model Dev.* **9**, 1937–1958 (2016).
63. Jungclaus, J. et al. *MPI-M MPI-ESM1.2-HR Model Output Prepared for CMIP6 CMIP Historical* v.20190710 (2019).
64. Saunders, R. et al. An update on the RTTOV fast radiative transfer model (currently at version 12). *Geosci. Model Dev.* **11**, 2717–2737 (2018).
65. Palchetti, L. et al. FORUM: unique far-infrared satellite observations to better understand how Earth radiates energy to space. *Bull. Am. Meteorol. Soc.* **101**, E2030–E2046 (2020).
66. Hocking, J. et al. *RTTOV v12 Users Guide* (NWP SAF, 2019); https://nwp-saf.eumetsat.int/site/download/documentation/rtm/docs_rttov12/users_guide_rttov12_v1.3.pdf
67. Kythe, P. & Puri, P. *Computational Methods for Linear Integral Equations* (Springer, 2011).
68. Dacie, S. et al. A 1D RCE study of factors affecting the tropical tropopause layer and surface climate. *J. Clim.* **32**, 6769–6782 (2019).
69. Eriksson, P., Buehler, S., Davis, C., Emde, C. & Lemke, O. ARTS, the atmospheric radiative transfer simulator, version 2. *J. Quant. Spectrosc. Radiat. Transf.* **112**, 1551–1558 (2011).
70. Buehler, S. A. et al. ARTS, the atmospheric radiative transfer simulator – version 2.2, the planetary toolbox edition. *Geosci. Model Dev.* **11**, 1537–1556 (2018).
71. Romps, D. M. An analytical model for tropical relative humidity. *J. Clim.* **27**, 7432–7449 (2014).
72. Roemer, F. E., Buehler, S. A., Brath, M., Kluft, L. & John, V. O. *Spectrally Resolved Fluxes and Feedbacks from Observations and Simulations (Version 2)* (WDC Climate, 2023); https://doi.org/10.26050/WDCC/FluxFeedb_ObsSim_v2

Acknowledgements

We acknowledge EUMETSAT for the IASI satellite data, ECMWF for the ERA5 reanalysis data and the World Climate Research Programme, the climate modelling groups and the Earth System Grid Federation (ESGF) for the CMIP6 data. This study contributes to the Cluster of Excellence 'CLICCS—Climate, Climatic Change, and Society', and to the Center for Earth System Research and Sustainability (CEN) of Universität Hamburg. F.E.R. was supported by the GRIPS project, funded by NOAA under grant NA20OAR4310375. Our thanks go to the ARTS radiative transfer community for their help with using ARTS and to O. Lemke for technical assistance.

Author contributions

S.A.B. proposed the idea for this study. F.E.R. conducted the analysis and drafted the manuscript. M.B. helped with developing the methodology, V.O.J. helped with acquiring and processing the satellite data and L.K. helped with setting up and interpreting the single-column simulations. All authors participated in outlining the study, discussing the results and revising the manuscript.

Funding

Open access funding provided by Universität Hamburg.

Competing interests

The authors declare no competing interests.

Additional information

Extended data is available for this paper at https://doi.org/10.1038/s41561-023-01175-6.

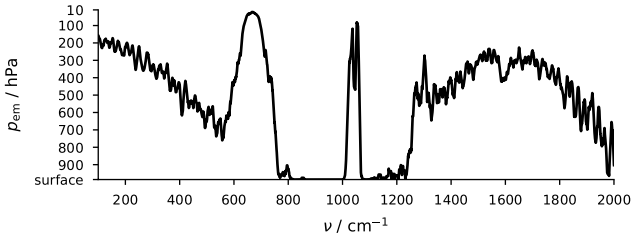
Supplementary information The online version contains supplementary material available at https://doi.org/10.1038/s41561-023-01175-6.

Correspondence and requests for materials should be addressed to Florian E. Roemer.

Peer review information *Nature Geoscience* thanks Nadir Jeevanjee, Qing Yue and Daniel Feldman for their contribution to the peer review of this work. Primary Handling Editor: Tom Richardson, in collaboration with the *Nature Geoscience* team.

Reprints and permissions information is available at www.nature.com/reprints.

https://doi.org/10.1038/s41561-023-01175-6



Extended Data Fig. 1 | Emission level p_{em} (10 cm^{-1} moving average) of spectral outgoing long-wave radiation. The emission level is calculated based on the MPI-ESM1-2-HR model. In the optically thin atmospheric window, the emission level is located at the surface. For better visibility, only the spectral range 100–2000 cm^{-1} is shown.

https://doi.org/10.1038/s41561-023-01175-6

Extended Data Table 1 | Long-wave feedback parameter λ as estimated by different studies

study	data source	methodology	λ / $\mathrm{W\,m^{-2}\,K^{-1}}$
Sherwood et al. (2020)	–	review	$-2.05 \pm 0.18^{a,b}$
Soden et al. (2008)	coupled models	long-term trend	-2.05^{a}
Huang et al. (2014)	coupled models	long-term trend	-1.98
Colman and Hanson (2017)	coupled models	long-term trend	-1.75 ± 0.40^{b}
Jeevanjee (2018)	1D model	long-term trend	-2.0^{a}
Kluft et al. (2019)	1D model	long-term trend	-2.33^{a}
Budyko (1969)	observations	regional variability	-2.26^{a}
Chung et al. (2010)	observations[c]	regional variability	-2.2^{a}
Chung et al. (2010)	coupled models	regional variability	-2.1^{a}
Koll and Cronin (2018)	observations	regional variability	-2.22^{a}
Forster and Gregory (2006)	observations[c]	interannual variability	-3.7 ± 0.9
Murphy et al. (2009)	observations[c]	interannual variability	-2.78 ± 0.80
Murphy et al. (2009)	observations[d]	interannual variability	-1.64 ± 0.84
Chung et al. (2010)	observations[c]	interannual variability	-2.4^{a}
Chung et al. (2010)	coupled models	interannual variability	-2.3^{a}
Dessler (2013)	observations[d]	interannual variability	-1.45 ± 0.73^{b}
Donohoe et al. (2014)	observations[d]	interannual variability	-2.0 ± 0.3
Trenberth et al. (2015)	observations[d]	interannual variability	-1.7 ± 0.3
Colman and Hanson (2017)	coupled models	interannual variability	-1.42 ± 0.82^{b}
This study	observations	interannual variability	-2.03 ± 0.005
Tsushima et al. (2005)	observations[c]	seasonal variability	-2.05 ± 0.17
Forster and Gregory (2006)	observations[c]	seasonal variability	-2.7 ± 1.2
Chung et al. (2010)	observations[c]	seasonal variability	-2.3^{a}
Chung et al. (2010)	coupled models	seasonal variability	-2.0^{a}
Tsushima and Manabe (2013)	observations[c]	seasonal variability	-2.09^{e}
Tsushima and Manabe (2013)	observations[d]	seasonal variability	-2.31^{e}
This study	observations	seasonal variability	-1.96 ± 0.002

[a]only including clear-sky feedbacks
[b]We calculate the error of the total λ by adding the errors of the individual feedbacks in quadrature.
[c]Earth Radiation Budget Experiment (ERBE)
[d]Clouds and the Earth's Radiant Energy System (CERES)
[e]We calculate $\lambda = \lambda_0 \cdot (1 - g)$ from the gain factor g, which quantifies by how much the absolute value of λ is reduced compared to the reference Planck feedback $\lambda_0 = -3.21\,\mathrm{W\,m^{-2}\,K^{-1}}$ (Tsushima and Manabe, 2013).

https://doi.org/10.1038/s41561-023-01175-6

Extended Data Table 2 | All-sky spectral long-wave feedback parameter λ_ν derived from observations by the IASI instrument

spectral band	spectral range cm^{-1}	seasonal variability $W\,m^{-2}\,K^{-1}$	interannual variability $W\,m^{-2}\,K^{-1}$
FIR H_2O	100–570	−0.27	−0.28
CO_2	570–770	−0.11	−0.32
window	770–990, 1080–1250	−1.25	−0.99
O_3	990–1080	−0.12	−0.21
MIR H_2O	1250–2000	−0.16	−0.19
combined H_2O	100–570, 1250–2000	−0.42	−0.47
total	100–2760	−1.96	−2.03

The λ_ν are derived from seasonal and interannual variability and integrated over different spectral bands. The λ_ν for wavenumbers $\nu < 645\,cm^{-1}$ are estimated using a prediction model (Methods). All errors are $< 0.005\,W\,m^{-2}\,K^{-1}$.

https://doi.org/10.1038/s41561-023-01175-6

Extended Data Table 3 | Simulated clear-sky spectral long-wave feedback parameter λ_ν integrated over different spectral bands

spectral band	spectral range cm^{-1}	seasonal variability $W\,m^{-2}\,K^{-1}$	interannual variability $W\,m^{-2}\,K^{-1}$	surface feedback $W\,m^{-2}\,K^{-1}$
FIR H_2O	100–570	−0.14	−0.32	−0.07
CO_2	570–770	−0.11	−0.32	−0.07
window	770–990, 1080–1250	−1.21	−1.11	−1.09
O_3	990–1080	−0.16	−0.17	−0.16
MIR H_2O	1250–2000	−0.11	−0.15	−0.06
combined H_2O	100–570, 1250–2000	−0.25	−0.47	−0.13
total	100–2760	−1.78	−2.12	−1.49

The λ_ν are derived from seasonal and interannual variability calculated from simulations based on the MPI-ESM1-2-HR model. The surface feedback is an estimate based on those simulations, calculated using Eq. (14) (Methods). All errors are < 0.004 $W\,m^{-2}\,K^{-1}$.

https://doi.org/10.1038/s41561-023-01175-6

Extended Data Table 4 | Simulated clear-sky spectral long-wave feedback parameter λ_ν derived from konrad simulations and integrated over different spectral bands

spectral band	spectral range cm^{-1}	$d\mathcal{R}/dT_s = +0.5\,\%\,K^{-1}$ $W\,m^{-2}\,K^{-1}$	$d\mathcal{R}/dT_s = \pm 0.0\,\%\,K^{-1}$ $W\,m^{-2}\,K^{-1}$	$d\mathcal{R}/dT_s = -0.5\,\%\,K^{-1}$ $W\,m^{-2}\,K^{-1}$
FIR H_2O	100–570	−0.11 (−0.14)	−0.19 (−0.19)	−0.27 (−0.24)
CO_2	570–770	−0.34 (−0.33)	−0.36 (−0.34)	−0.38 (−0.36)
window	770–990, 1080–1250	−0.93 (−0.85)	−0.98 (−0.91)	−1.04 (−0.96)
O_3	990–1080	−0.19 (−0.18)	−0.20 (−0.18)	−0.20 (−0.19)
MIR H_2O	1250–2000	−0.12 (−0.12)	−0.15 (−0.14)	−0.18 (−0.16)
combined H_2O	100–570, 1250–2000	−0.23 (−0.27)	−0.34 (−0.33)	−0.45 (−0.40)
total	100–2760	−1.75 (−1.68)	−1.94 (−1.83)	−2.14 (−1.97)

Shown are the results from three different experiments: Increasing relative humidity $\mathcal{R}$ with near-surface air temperature Ts (left column), constant $\mathcal{R}$ with Ts (middle column) and decreasing $\mathcal{R}$ with Ts (right column). The results are shown for both a C-shaped $\mathcal{R}$ profile as shown in Fig. 3a and a vertically uniform $\mathcal{R}$ profile (numbers in parentheses).